Radiative Hydrodynamic Simulations of HD209458b: Temporal Variability

Ian Dobbs-Dixon[1,2], Andrew Cumming [1], D.N.C Lin [3,4]

[1]*Department of Physics, McGill University, Montreal, H3A 2T8 Canada*

[2]*Department of Astronomy, Box 351580, University of Washington, Seattle, WA 98195*

[3]*Department of Astronomy and Astrophysics, University of California, Santa Cruz, CA 95064, USA*

[4]*Kavli Institute of Astronomy & Astrophysics, Peking University, Beijing, China*

ABSTRACT

We present a new approach for simulating the atmospheric dynamics of the close-in giant planet HD209458b that allows for the decoupling of radiative and thermal energies, direct stellar heating of the interior, and the solution of the full 3D Navier Stokes equations. Simulations reveal two distinct temperature inversions (increasing temperature with decreasing pressure) at the sub-stellar point due to the combined effects of opacity and dynamical flow structure and exhibit instabilities leading to changing velocities and temperatures on the nightside for a range of viscosities. Imposed on the quasi-static background, temperature variations of up to 15% are seen near the terminators and the location of the coldest spot is seen to vary by more than 20°, occasionally appearing west of the anti-solar point. Our new approach introduces four major improvements to our previous methods including simultaneously solving both the thermal energy and radiative equations in both the optical and infrared, incorporating updated opacities, including a more accurate treatment of stellar energy deposition that incorporates the opacity relevant for higher energy stellar photons, and the addition of explicit turbulent viscosity.

Subject headings: hot-Jupiters, atmospheric dynamics, radiative transfer

1. Introduction

Close in gas-giant planets have by now become a familiar part of the growing family of extrasolar planets. Their short period orbits and proclivity for transiting has made them

the target of numerous observational campaigns and our knowledge of their structure and composition has increased dramatically over the past few years. The intense irradiation they receive from their host star dominates the energy budget of the atmosphere and drives supersonic flows unlike any seen in our own solar system. However, despite their prevalence and important role in constraining a wide range of planetary models, fundamental questions about the dynamical behavior of their atmospheres remain, crucial for interpreting observations.

There have been a number of different groups working to understand the dynamical redistribution of energy in close-in irradiated planets utilizing a wide range of approaches. Because of the breadth of these methods, interpreting the results and understanding their implications can be quite confusing. Detailed comparisons of many of the models in the literature have been presented previously (Dobbs-Dixon & Lin 2008; Showman et al. 2008b; Goodman 2008) and we will not attempt to repeat those discussions here but rather briefly place this present study in context. In a general sense, the approaches taken to this problem can be categorized using two criteria: the approach to radiation and the approach to dynamics. Both components are extremely important to include in any model. Energy transport, including radiation *and* advection, determines the distribution of thermal properties where as pressure gradients and gravity regulate thermal currents throughout the planet (Burkert et al. 2005). A self consistent treatment of both processes is required to determine the gas flow pattern and emerging radiative spectra.

Approaches utilized for radiation to date include relaxation methods (*i.e.* Newtonian heating) (Showman & Guillot 2002; Showman et al. 2008a; Cooper & Showman 2005, 2006; Langton & Laughlin 2007, 2008; Menou & Rauscher 2008; Rauscher & Menou 2009), kinematic constraints designed to represent incident flux (Cho et al. 2003, 2008; Rauscher et al. 2008), 3D flux-limited diffusion (Burkert et al. 2005; Dobbs-Dixon & Lin 2008), or 1D frequency dependent radiative transfer (Showman et al. 2009). Approaches to the dynamical portion of the model have included solving the equivalent barotopic equations (Cho et al. 2003, 2008; Rauscher et al. 2008), the shallow water equations (Langton & Laughlin 2007, 2008), the primitive equations (Showman & Guillot 2002; Showman et al. 2008a, 2009; Cooper & Showman 2005, 2006; Menou & Rauscher 2008; Rauscher & Menou 2009), and Euler's equations (Burkert et al. 2005; Dobbs-Dixon & Lin 2008).

Ideally we would integrate the full Navier-Stokes equations coupled to a 3D frequency dependent radiative transfer model. However, computational resources are limited, and simulations of this type take considerable time. Thus, to our knowledge the approach of all groups to date has been to choose one approach to dynamics and one to radiation, necessarily compromising on one or the other. For the results presented here we have chosen to utilize a two-frequency, 3D flux-limited model coupled to the full 3D compressible Navier-Stokes

equations. Our goal in this study is to understand the details of atmospheric dynamics and energy transfer in highly irradiated environments which are not spherically symmetric. Our new approach to the radiation flux reproduces many of the general features of frequency-dependent approaches. Most importantly, it allows for energy deposition at a depth corresponding to the optical photosphere. The depth of deposition controls much of the subsequent dynamics and a bolometric approach to the energy transfer is all that is needed.

The plan of the paper is as follows; Section (2) describes our numerical approach, concentrating on the improvements to our methods from our previous paper (Dobbs-Dixon & Lin 2008). Primarily, this improvement lies in the treatment of the energy equation in which we track the energetic components separately. In addition, we use updated opacities calculated for infrared and optical components independently. In Section (3) we present results for the well known HD209458b. We begin by illustrating the radiative solution, reproducing many of the important features of the pressure-temperature profiles from more detailed 1D models. We then present a number of aspects of the underlying flow and atmospheric structure for a range of viscosities. Viscosity plays an important role in both regulating flow velocities and providing viscous heating. For a range of viscosities, our simulations exhibit dynamical variations that give rise to changing temperature distributions across the photosphere. Section (3.3) presents several aspects of this exo-weather, in particular changes we expect to see from multiple observations. Finally, several questions regarding the nature of the energy flow throughout the atmosphere have recently been posed by Goodman (2008). To address this, in Section (4) we discuss the role of viscosity in determining the entropy distribution throughout the atmosphere, and the relative fluxes of kinetic energy, enthalpy, and radiation from day to nightside. We conclude with a discussion in Section (5).

2. Model Description

We model the planetary atmosphere using a three-dimensional radiative hydrodynamical model in spherical coordinates (r, ϕ, θ). In addition to the numerical techniques utilized in solving the hydrodynamical portion of the code described in Dobbs-Dixon & Lin (2008), we have added explicit viscosity terms to our equations in the form described by Kley & Hensler (1987). Significant changes to the radiative component of our atmospheric model have also been implemented. In addition to updated opacities (Sharp & Burrows 2007), we have decoupled the radiative and thermal energy components and introduced a multi flux channel approach for the radiative energy component in a manner similar to the approach of Howell & Greenough (2003).

The fully compressible three dimensional Navier-Stokes equation for the motion of the

fluid is given by

$$\frac{\partial \mathbf{u}}{\partial t} + (\mathbf{u} \cdot \nabla) \mathbf{u} = -\frac{\nabla P}{\rho} + \mathbf{g} - 2\mathbf{\Omega} \times \mathbf{u} - \mathbf{\Omega} \times (\mathbf{\Omega} \times \mathbf{r}) + \nu \nabla^2 \mathbf{u} + \frac{\nu}{3} \nabla (\nabla \cdot \mathbf{u}) \qquad (1)$$

where $\mathbf{u}$ is the three-dimensional velocity, ρ and P are the gas density and pressure, and Ω is the rotation frequency. The gravitational acceleration, $\mathbf{g}$ is taken here to be purely radial. $\nu = \eta/\rho$ is the constant kinematic viscosity, proportional to η, the dynamic viscosity. We have neglected the coefficient for the bulk viscosity. For further details on the treatment of the viscous terms we direct the reader to Kley & Hensler (1987). Explicit viscosity is supplemented by an additional artificial viscosity for the accurate treatment of shocks. The functional form of this term is identical to that in the ZEUS code (Stone & Norman 1992). Equation (1) is supplemented by the continuity equation, given by

$$\frac{\partial \rho}{\partial t} + \nabla \cdot (\rho \mathbf{u}) = 0. \qquad (2)$$

The equation for internal energy of the gas can be written as

$$\left[\frac{\partial \epsilon}{\partial t} + (\mathbf{u} \cdot \nabla)\epsilon \right] = -P \nabla \cdot \mathbf{u} - \sum_i \rho c \kappa_{P,i} \left(\frac{j_i}{c \kappa_{P,i}} - E_{R,i} \right) + D_\nu, \qquad (3)$$

The quantity proportional to j_i represents the photons added to the i-th radiation energy density, while the term on the right-hand side proportional to $E_{R,i}$ represents those absorbed by the gas. $\kappa_{P,i}$ is the Planck opacity, defined below. Ignoring non-coherent scattering, these terms represent either impinging radiation or interactions with the surrounding gas. In the above $\epsilon = c_v \rho T$ is the internal energy density, c_v is the specific heat, and $D_\nu = (\mathbf{S}\nabla) \mathbf{v}$ is the viscous dissipation function. The components of the viscous stress tensor $\mathbf{S}$ are detailed in Kley & Hensler (1987) or Milhalas & Milhalas (1984). With the exception of the isotropic assumption for j_ν and κ_ν (used during the angular integration of Equation (4) below) and neglecting scattering, this set of equations is completely general and can be expanded to an arbitrary number of frequency bins.

In addition to the internal energy of the gas we must also derive an expression for the radiation energy. For this consider a simplified frequency dependent model with two frequency ranges. We can write the radiative transfer equation as

$$\frac{1}{c} \frac{\partial I_\nu}{\partial t} + \hat{\mathbf{k}} \cdot \nabla I_\nu = \rho \left(\frac{j_\nu}{4\pi} + \kappa_\nu^{scat} \Phi_\nu^{scat} \right) - \rho \kappa_\nu I_\nu. \qquad (4)$$

In the above I_ν is the specific intensity, j_ν is the emissivity, and $\kappa_\nu = \kappa_\nu^{abs} + \kappa_\nu^{scat}$ is the total opacity; the sum of the absorption and scattering opacities. The intensity of photons scattered into the beam is given by $\Phi_\nu^{scat} = \int \phi_\nu \left(\mathbf{k}', \hat{\mathbf{k}} \right) I_\nu \left(\mathbf{k}' \right) d\Omega'$, where $\phi_\nu \left(\mathbf{k}', \hat{\mathbf{k}} \right)$ is the

scattering probability density between the $\hat{\mathbf{k}}$ and $\mathbf{k}'$ beams. Integrating Equation (4) over angle, we define the moments as $(cE_{R,\nu}, \mathbf{F}_\nu) = \int \left(1, \hat{\mathbf{k}}\right) I_\nu d\Omega$, where $E_{R,\nu}$ and $\mathbf{F}_\nu$ are the frequency dependent radiation energy density and flux respectively.

We now identify the first frequency interval with the incoming stellar radiation. This is characterized by the larger $T_\star$, and peaks in the optical. The second frequency interval then represents the local re-radiated energy, characterized by the local temperature T. This peaks in the infrared for the problem of interest here. Addressing the impinging stellar photons first (group 1) we assume that the atmospheric gas does not emit in this wave-band, implying $j_1 = 0$. To find an expression for E_1, the stellar energy absorbed by the gas, we return to the full radiative transfer equation. Allowing only absorption, and neglecting temporal variations, Equation (4) for the intensity of the stellar radiation can be written simply as

$$\frac{dI_\star}{dr} = -\rho\kappa_\star I_\star, \tag{5}$$

with solution $I_\star = I_{\star,0}\exp\left[-\tau_\star\right]$. We have denoted this frequency interval with the subscript $\star$. The stellar heating term in Equation (3) can then be written as

$$E_{R,1} = E_\star = \frac{1}{c}\int I_\star d\Omega = \frac{1}{c}I_{\star,0}e^{-\tau_\star} = WaT_\star^4 e^{-\tau_\star}, \tag{6}$$

where we have explicitly assumed that this radiation is *not* isotropic but rather flows radially from the central star. The factor W accounts for the attenuation of the stellar energy and is inversely proportional to the square of the semi-major axis. The optical depth for incoming stellar radiation is given by $\tau_\star$.

We now return to Equation (4) for the local, re-processed radiation (frequency interval 2), which peaks in the infrared for this problem. Integrating Equation (4) over angle and frequency, dropping the subscript 2, assuming the gas radiates this energy isotropically and is in local thermodynamic equilibrium (*i.e.* $j = B\kappa$), the radiative energy component can be expressed as,

$$\frac{\partial E_R}{\partial t} + \nabla \cdot \mathbf{F} = \rho\kappa_P(T, P)\left[B(T) - cE_R\right]. \tag{7}$$

In the above integration we have assumed that j_ν and κ_ν are isotropic. The local radiative energy density E_R is evolved independently from the thermal component using this equation, with the term $B(T) = 4\sigma T^4$ linking it to the gas.

Combining Equations (3) and (6), the final thermal energy equation is given by

$$\left[\frac{\partial\epsilon}{\partial t} + (\mathbf{u}\cdot\nabla)\epsilon\right] = -P\nabla\cdot\mathbf{u} - \rho\kappa_P(T, P)\left[B(T) - cE_R\right] + \rho\kappa_\star(T, P)F_\star e^{-\tau_\star} + D_v. \tag{8}$$

The second term on the left accounts for the advection of thermal energy throughout the planet, the first term on the right is the compressional heating term, the term proportional

to $B(T) - cE_R$, represents the exchange of energy between the thermal and radiative components through the emission and absorption of the low energy photons, and $\rho \kappa_\star(T, P) F_\star e^{-\tau_\star}$ represents the higher energy stellar photons absorbed by the gas. The stellar flux at the planet's dayside surface will be

$$F_\star = \sigma T_\star^4 \left(\frac{R_\star}{a} \right)^2 [\cos(\theta) \cos(\phi)], \tag{9}$$

where θ and ϕ are latitude and longitude on the planet's surface.

There are two final ingredients necessary for solving the energy balance in the atmosphere; a prescription for the opacity and a closure relation linking the flux $\mathbf{F}$ back to the radiation energy density. Here we utilize the three dimensional flux-limited diffusion (FLD) approximation of Levermore & Pomraning (1981), where

$$\mathbf{F} = -\lambda \frac{c}{\rho \kappa_R(T, P)} \nabla E_R. \tag{10}$$

The Rosseland opacity is given by $\kappa_R(T, P)$, and λ is a temporally and spatially variable flux limiter providing the closure relationship between flux and radiation energy density. The functional form of λ is given by

$$\lambda = \frac{2 + R}{6 + 3R + R^2}, \tag{11}$$

where

$$R = \frac{1}{\rho \kappa_R(T, P)} \frac{|\nabla E_R|}{E_R}. \tag{12}$$

FLD has been utilized in a wide range of astrophysical applications and allows for the simultaneous study of optically thick and optically thin gas, correctly reproducing the limiting behavior of the radiation at both extremes. In the optically thick limit the radiation energy can be expressed as $E = aT^4$, and the flux becomes the standard radiative diffusion equation,

$$\mathbf{F} = -\frac{4acT^3}{3\rho \kappa_R(T, P)} \nabla T. \tag{13}$$

In the optically thin streaming limit, Equation (10) becomes

$$|\mathbf{F}| = cE_R. \tag{14}$$

Between these limits, Equation (11) approximates the full wavelength dependent radiative transfer models of Levermore & Pomraning (1981).

There are three frequency averaged opacities appearing in Equations (7), (8), and (10): $\kappa_P(T, P)$, $\kappa_\star(T, P)$, and $\kappa_R(T, P)$. The importance of differing absorption opacity and emissivity was first noted by Hubeny et al. (2003) but not widely appreciated until the discovery of the stratosphere of HD209458b (Knutson et al. 2008). The modeling of HD209458b

(Burrows et al. 2007, *e.g.*) suggests a thermal inversion in the upper atmosphere largely due to the differing opacities. Here we include these effects within the framework of frequency averaged opacities. 3D frequency dependent radiative transfer coupled to the full 3D Navier-Stokes equations would be the ideal tool for these calculations; unfortunately, to our knowledge no such calculations exist to date. Although our models do not contain the full wavelength dependent opacities of one-dimensional radiative models, with the addition of multiple average opacities and the radiative energy equation we are able to capture many of the essential features that appear in such models. The energetics powering the underlying dynamics is well represented by an average approach. Moreover, this approach allows us to still solve the full three dimensional Navier Stokes Equations with reasonable computational requirements. Our previous atmospheric models (Dobbs-Dixon & Lin 2008) not only took the radiative and thermal temperatures to be equal but also assumed that all three of these opacities were equivalent. Of particular importance, our new approach modifies the radial location that the stellar energy is initially deposited and the winds are launched. The unfortunate side-effect is that we cannot produce detailed spectra directly from these models. However, it is possible to post-process the pressure-temperature profiles derived here using a one-dimensional radiative transfer code, which will be presented elsewhere.

Planck and Rosseland mean opacities are defined in the usual manner, but the temperature at which the spectra is evaluated is critical. The local Planck mean for the low-energy photon group is given by

$$\kappa_P(T, P) = \frac{\int \kappa_{\nu, ns}(T, P) B_\nu(T) \, d\nu}{\int B_\nu(T) \, d\nu}, \tag{15}$$

while the Planck mean for the high-energy photon group is defined as

$$\kappa_\star(T, P) = \frac{\int \kappa_{\nu, ns}(T, P) J_\nu(T_\star) \, d\nu}{\int J_\nu(T_\star) \, d\nu}. \tag{16}$$

The frequency dependent opacity is given by κ_ν, and the subscript *ns* indicates scattering processes are neglected when calculating the wavelength dependent opacities. In principle, the impinging radiation can differ from a black-body, but for our purposes we set $J_\nu(T_\star) = B_\nu(T_\star)$. Finally, the Rosseland mean for the low-energy group is given by

$$\kappa_R(T, P)^{-1} = \frac{\int \kappa_{\nu, s}^{-1}(T, P) \frac{\partial B_\nu(T)}{dT} d\nu}{\int \frac{\partial B_\nu(T)}{dT} d\nu}. \tag{17}$$

Here wavelength dependent opacities include the effect of scattering (subscript *s*). In the calculations presented here we use the wavelength dependent opacities as described in Sharp & Burrows (2007)

Burrows et al. (2008) find that matching the spectral data from HD209458b requires the addition of a supplemental, unknown uniform opacity source of $\kappa_e = 0.1 \text{cm}^2/\text{g}$ at pressures below 0.03 bars. The source of this additional opacity is currently unknown. Some of the leading contenders are titanium oxide (TiO) and vanadium oxide (VO) (Hubeny et al. 2003). However, though TiO and VO may indeed be the dominate source of opacity in the upper atmosphere at high temperatures ($T \gtrsim 1500$K), its abundance remains an outstanding question. Spiegel et al. (2009) find, in the absence of abnormally large vertical mixing coefficients, it is likely that VO settles out of the upper atmosphere and does not play a role in producing thermal inversions. Zahnle et al. (2009) suggest S_2 and S_3 as another potential source of high altitude absorption. Rather then introduce the complex temperature and pressure dependence of an unknown amount of TiO, VO, S_2, or S_3, our opacities *do not* contain these explicit compounds. Instead we follow Burrows et al. (2008) and augment the Planck opacities in the upper atmosphere with the straightforward κ_e parameterization. The value of κ_e is simply a fit to current observations and is easily modified for studying other situations.

3. Energy Flow Throughout the Planetary Atmosphere

In this section we present simulations of the full radiative-hydrodynamical solutions of Equations (1), (2), (7), and (8) for conditions meant to represent the close-in giant planet HD209458b. To this end, the orbital and (assumed) rotation periods of the planet are $P = 3.52$days, corresponding to a semi-major axis of 0.047 AU. The host star is taken to have a radius of $1.15 R_\odot$ and a temperature of 6030K (Mazeh et al. 2000). Although observable parameters are chosen from the literature, we have not attempted to tune the models to fit observed spectra or light-curves, with the exception of the extra opacity source added (see Section (2)). Our goal here is to explore general properties of atmospheric flow; specific models with tuned parameters will be presented elsewhere. These results can be considered representative of flows as you would see on planets similar to HD209458b.

We solve the problem in 3D spherical coordinates with a standard resolution of $(N_r, N_\phi, N_\theta) = (60, 160, 64)$. Due to the decreasing grid size near the pole, and the associated Courant time-step constraint, we limit the latitudinal extent of our grid to $\pm 70^o$. These boundaries are impenetrable and slip-free, and the flux is set to zero. The role of these artificial poles on the overall flow is difficult to characterize and is an unfortunate side effect of the chosen coordinate system. We have run tests changing $|\theta_{max}|$ by $10°$ and have observed little effect on the overall atmospheric structure. However, this test is not conclusive. A more concrete discussion of the effect of this boundary requires eliminating this boundary by means of a 'polar-patch' which we hope to include in future models.

All simulations are initialized with the static one-dimensional equilibrium pressure-temperature profiles as calculated in Burrows et al. (2007). As discussed below in Section (3.1), we then solve the radiative portion of the energy equations, subject to the non-symmetric stellar irradiation until the simulation reaches radiative equilibrium. Dynamical results, discussed in Section (3.2) are initialized with this static radiative-equilibrium model. The gas at the inner boundary is assumed to be optically thick ($E_R = aT^4$) and its properties spherically symmetric while the boundary is assumed to be impenetrable and slip free. We set a spherically symmetric radiative flux and calculate the temperature gradient with Equation (13). The pressure at the inner boundary is set well within the spherically symmetric convective interior, allowing us to both avoid any influence of the choice of inner velocity boundary conditions on the upper atmospheric flow and allow for the interaction between the convective interior and irradiation induced dynamics. A set of less restrictive inner boundary conditions are needed to determine the influence of stellar irradiation on convection, cooling, and the quasi hydrostatic contraction rates of hot Jupiters. Such simulations will be presented elsewhere. A movable outer boundary (*not* associated with either the optical or infrared photospheres) is located at a density of 10^{-9}g/cm^3, through which we assume a constant outward radiative flux ($dF_R/dr = 0$) through an optically thin gas, given by Equation (14). Given the negligible effect of dynamics at the lowest pressures, the gas temperature at the outer boundary is set to its thermal steady-state value with Equation (18), given below.

3.1. Radiative Solution

Before including the dynamical portion of the code, we first allow the simulation to come to radiative equilibrium. This is accomplished by solving the energy equations given by Equations (7) and (8) with $\mathbf{u} = 0$. The temperature profiles are shown in Figure (1). The solid line denotes the gas temperature T and the dashed line denotes the radiative energy E_R. Decoupling the energy into thermal and radiative components is a crucial element to account for when studying an irradiation induced upper atmospheric temperature inversion, and is clearly evident near the stellar photosphere where E_R remains roughly constant. Also shown in Figure (1) are the locations of the infrared and optical photospheres and the (scaled) direct stellar heating term $\rho\kappa_\star(T, P) F_\star e^{-\tau_\star}$. The extent of the temperature inversion is clearly associated with the deeper optical photosphere and the resulting extent of the heating term. Our radiative pressure-temperature profiles are quite similar to those in Burrows et al. (2007), with the exception of the ad-hoc energy sink they add to the dayside at high pressures to mimic the effects of dynamics. This energy sink decreases the temperature at depth, producing a secondary inversion in their models. This feature is seen self-consistently in our dynamical simulations (Section (3.2)).
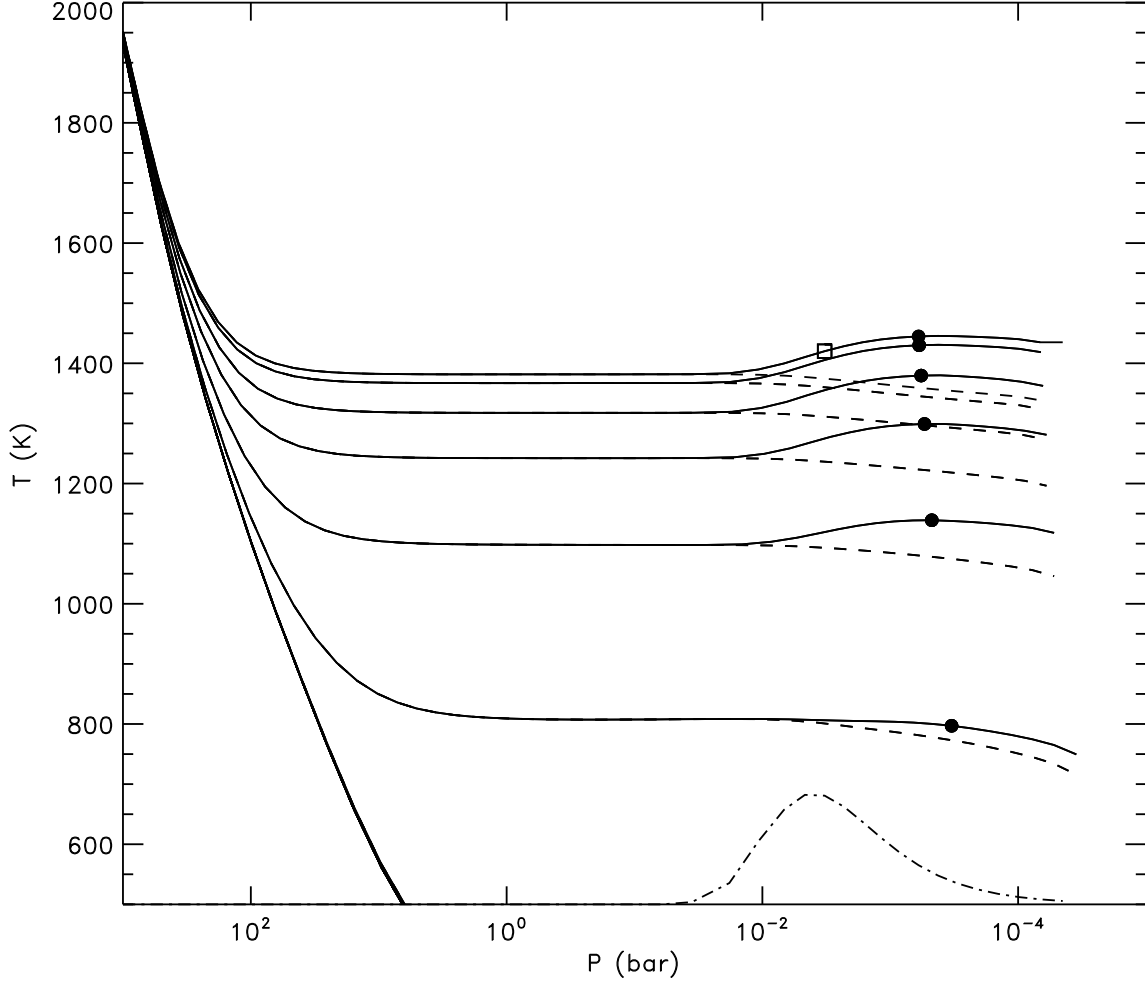
Fig. 1.— The temperature as a function of pressure for a purely radiative solution (solid line) from the sub-stellar point to anti-stellar point. The dashed line shows $(E_R/a)^{1/4}$ and illustrates the decoupling of thermal and radiative energies near the photosphere. Solid points denote the location of the infrared photosphere, while the square shows the location of the optical photosphere on the dayside. Also shown (dot-dash line) is the extent of the stellar heating $\rho \kappa_\star \left(T, P\right) F_\star e^{-\tau_\star}$.

To understand the behavior of the temperature at low optical depths consider the steady-state behavior of Equation (8) for zero velocity. In this case the gas temperature can be expressed as

$$T = \left[\frac{E_R}{a} + \gamma^4 \frac{F_\star}{4\sigma} e^{-\tau_\star} \right]^{1/4},$$ (18)

Local equilibrium between absorption and emission requires that the gas temperature be greater then $\left(\frac{E_R}{a} \right)^{1/4}$. In the above, γ is the ratio of Planck opacities evaluated for the stellar and local fluxes as defined by Hubeny et al. (2003) as

$$\gamma^4 \equiv \frac{\kappa_\star(T, P)}{\kappa_P(T, P)}.$$ (19)

The role that the two opacities play in creating a temperature inversion is apparent in Equation (18), the nature of which depends sensitively on the behavior of γ with depth; an inversion requires $\gamma^4 e^{-\tau_\star}$ to increase outward, while a temperature peak in the outer atmosphere (seen in some simulations not presented here) requires a peak in this quantity. If the opacity is such that regions exist above the optical photosphere with $\gamma > 1$, the gas temperature can easily become super-heated, exceeding the equilibrium temperature calculated from Equation (9).

3.2. Mean Dynamical Solution

In this section we present the full radiative hydrodynamical simulations for HD209458b. All dynamical simulations are initialized with the zero velocity radiative equilibrium results discussed in Section (3.1). Fluid velocities are initially artificially damped then slowly ramped to their full values to avoid spurious oscillations or shocks associated with the initialization. As discussed below, several aspects of the flow and temperature distribution have significant time varying components. Results shown in this section are averaged over approximately one day, in hopes of representing mean flow properties. Results presented here are taken from simulations that have run for a minimum of 100 simulated days. Mean temperature and velocity distributions appear to have stabilized by this point. Section (3.3) presents the superimposed time-varying characteristics.

To explore the role of viscosity we have repeated our analysis for a range of kinematic viscosities, shown in Table (1). We will refer to runs with different viscosities using the notation S1-S4. In the absence of more detailed knowledge of the detailed dissipative processes (*e.g.* small scale instabilities or turbulence) we take the kinematic viscosity to be a constant. Also listed in Table (1) is the characteristic value of $\alpha_{eff,ph} = \nu/(c_s H)$ at the photosphere for each simulation, where H_p is the pressure scale-height at the photosphere. Although

11

we do not utilize the α-prescription, it is a useful way to normalize our chosen viscosity values. Our viscosity is assumed to be ultimately related to the generation of turbulence and the cascade of this energy to small length scales. Turbulence may be generated through many processes including various shear instabilities (associated for example with overturning Kelvin-Helmholtz instabilities), waves acting throughout the atmosphere (both inertial waves in the convective regions and Hough modes in the radiative regions (Ogilvie & Lin 2004)), and shocks generated within the interacting flow. Given the limited resolution achievable in dynamical simulations, the cascade of turbulence to scales smaller than our grid size and the subsequent damping of that energy must necessarily be represented by a sub-grid model. Penev et al. (2008) have recently shown that turbulent flows can be well represented by such an effective viscosity coefficient, such as in the final two terms in Equation (1). Given the uncertainty of the sub-grid physics, we have chosen to run models for a range of ν. As is explained below the values bracket a critical viscosity ν_{crit}, for which we expect viscous effect to be (sub)dominate. In addition, there is some amount of observational motivation for this choice from observations of Jupiter's photochemistry. Moses et al. (2005) show that the eddy diffusion coefficient for particles at pressures of 10^{-4}bars to be $10^5 - 10^6$cm^2/s. Presumably momentum diffusion will be more effective than species diffusion.

Figure (2) shows the temperature at the infrared photosphere for simulations with a range of viscosities. Temperatures range from 1400K to 440K at the photosphere. The hottest photospheric point lies slightly east ($\phi > 0$) of the sub-stellar point in all simulations, while the coolest points are at higher latitudes (both above and below the equator) on the nightside. Along the equator, the location of the coolest point depends on viscosity, lying east of the anti-stellar point ($\phi > \pi$) for the low viscosity runs S3 and S4. For S2, viscous heating associated with the converging flows drives oscillations in the location of the coldest point (see Section (3.3)). The highest viscosity run (S1) exhibits very little flow on the nightside and the coldest point remains very near the anti-stellar point.

Simulation	ν (cm^2/s)	$\alpha_{eff,ph}$	$H_{p,ph}$ (km)	peak v_ϕ (km/s)
$S1$	10^{12}	10^{-1}	330	0.8
$S2$	10^{10}	10^{-3}	360	4.5
$S3$	10^{8}	10^{-5}	360	5.3
$S4$	10^{4}	10^{-9}	360	5.7

Table 1: Values of kinematic viscosity used for the simulations presented here. For reference we also quote an average effective alpha-parameter and pressure scale-height all calculated at the photosphere. Peak velocities, shown in the last column, increase with decreasing viscosity.

Figure (3) illustrates the total speed at the infrared photosphere. Here again, the simulations exhibit a range of behaviors for the varying viscosity, with the highest viscosity (S1) keeping velocities below 1km/s. For the other simulations, as fluid moves from the sub-stellar point in the eastward direction (*ie* to the right in the figures) it is funneled toward the equator, while westward moving material is pushed toward the poles. In an inertial frame, planet spins from the west toward the east with an angular frequency $\Omega = 2.1 \times 10^{-5}$ s^{-1}. Eastward and westward winds with 5 km s^{-1} in the co-rotating frame introduce a local change in the azimuthal angular frequency $\Delta\Omega = \pm 7 \times 10^{-6}$ s^{-1} or $\pm 0.3\Omega$. The result is the formation of a banded pattern, with jet-like structures. The exact mechanism for the formation of jets both in these simulations and in solar system atmospheres remains an outstanding question. The anti-symmetry appears to be associated with the rotation of the planet, perhaps related to the asymmetry of the Coriolis force (For more detailed plots of this phenomena see Dobbs-Dixon & Lin (2008)). Non-rotating simulations, presented in Dobbs-Dixon & Lin (2008), show a very symmetric flow pattern despite large wind speeds. Despite the high velocity flows, the role of rotation in shaping the flow is not wholly unexpected as the the Rossby number, given by the ratio of the advective and rotation terms in Equation (1), is of order unity throughout most of the atmosphere in our simulations. Given the highly unstable nature of the symmetric flow in a non-rotating planet it seems that only a slight imposed asymmetry is necessary to form the banded structure seen in Figure (3).

Westward moving material at high latitudes always reaches a stagnation point west of the anti-stellar point as it encounters the opposing flow near $\phi \sim 140°$. At this point the fluid subducts under its counter-part, slowing considerably as it crosses down isobars to higher pressures and continues around the planet. The behavior of fluid moving in the eastward direction at the equator varies with viscosity. For S2, eastward flowing fluid also subducts under the opposing flow, much in the same manner as the westward moving fluid. However, for S3 and S4 the fluid is able to form a circumplanetary equatorial jet at roughly a single pressure level. Peak velocities, increasing with decreasing viscosity to over 5km/s for S4, are found just east of the anti-stellar point, but quickly decelerate as it passes back up the pressure gradient to the dayside. For reference the sound-speed at the photosphere ranges from 1.4km/s on the nightside to 2.9km/s on the dayside, implying the flow velocities can reach Mach 3.3 in the equatorial jet. Although S3 and S4 form and maintain a equatorial surface circumplanetary jet, there is still significant cooling of the flow after it passes the terminator, as can be seen in Figure (2).

To illustrate the subduction of material at the stagnation points, we show the azimuthal velocity at the equator ($\theta = 0$) and high latitudes ($\theta = 35°$) as a function of pressure for S2 and S3 in Figure (4). In both simulations, the wind is launched at low pressures and is accelerated as it passes across the terminators ($\phi = 90°$ and $270°$). These figures also clearly illustrate that subduction of fluid occurs for all but the low viscosity simulations at the
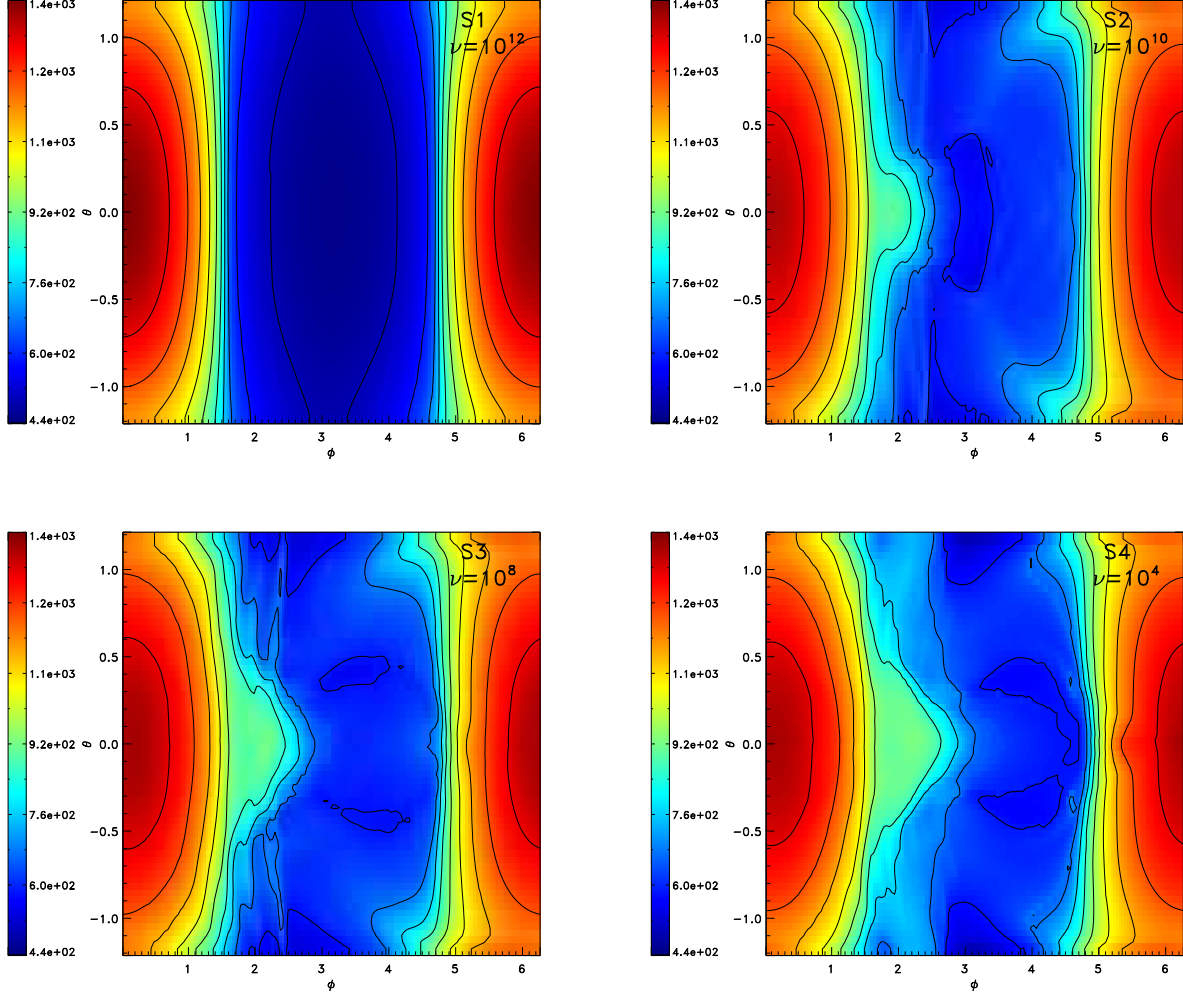
Fig. 2.— The temperature at the photosphere for simulations with varying viscosities. Viscosities for upper-left, upper-right, lower-left, and lower-right are 10^{12}, 10^{10}, 10^8, and $10^4 \mathrm{cm}^2/\mathrm{s}$ respectively. The center of each graph is located at the anti-stellar point $(\phi, \theta) = (\pi, 0)$ and the equator $(\theta = 0)$ runs horizontally through the center. For $10^{12} \mathrm{cm}^2/\mathrm{s}$, the lack of advection keeps the entire nightside cool, while for the other simulations advection significantly alters the temperature structure near the terminators $(\pi/2$ and $3\pi/2)$ and across the nightside.
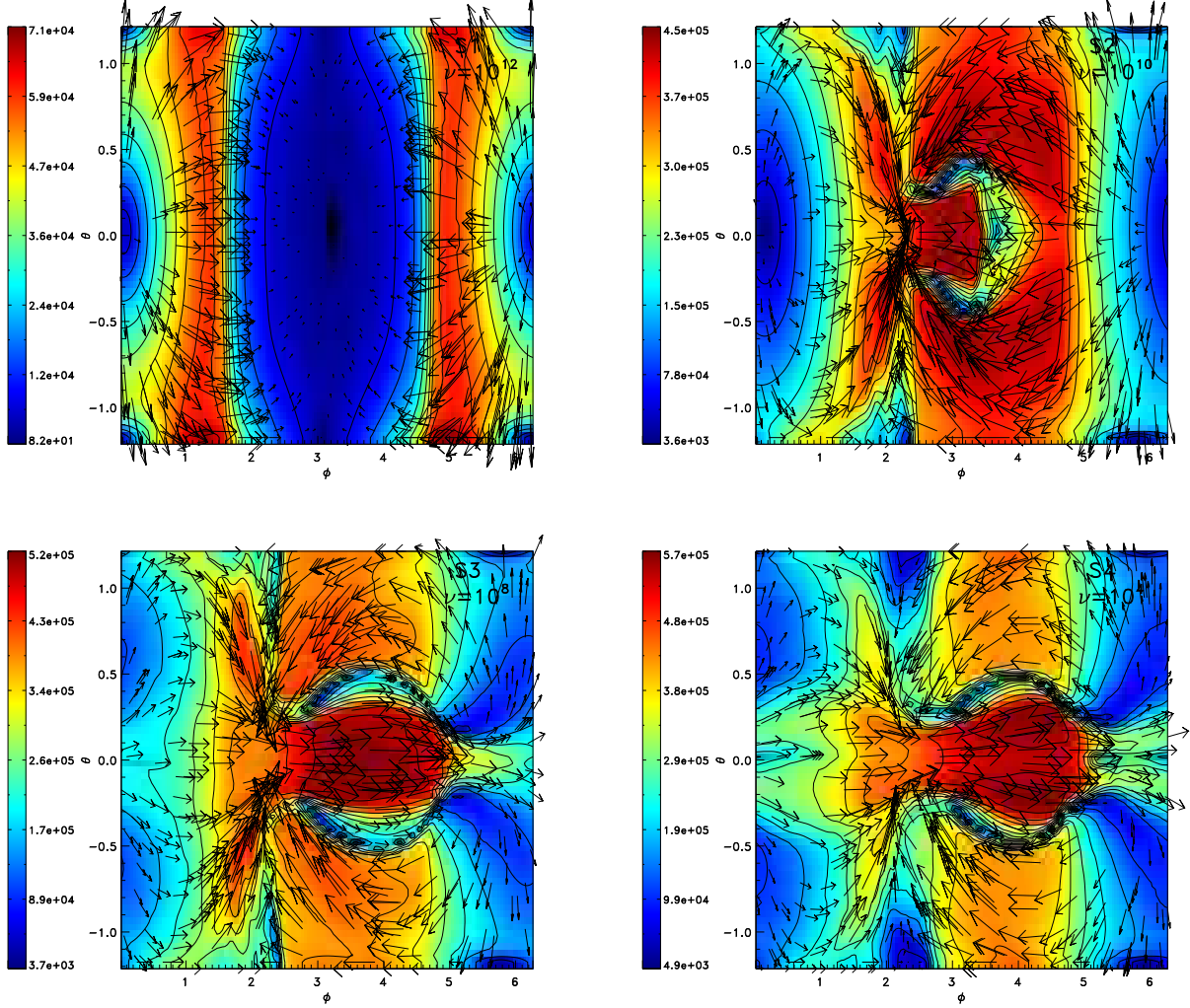
Fig. 3.— The total speed ($v = \sqrt{u_r^2 + u_\phi^2 + u_\theta^2}$) in cm/s at the photosphere for simulations with varying viscosities as in Figure (2). Over-plotted are velocities across the photosphere, with the arrow length proportional to velocity magnitude. Very little flow is found for high viscosity, while supersonic flows are found for the other simulations. The behavior of the jets also depends on viscosity, exhibiting both circumplanetary rotation and subduction.

equator. For example, in the upper left-hand plot of Figure (4) the peak velocity of eastward moving material (positive v_ϕ) shifts from pressures near 10^{-4} bars down to pressures near 10^{-1} bars near the opposite terminator ($\phi = 3\pi/2$). The peak velocities of the opposing westward fluid remain at low pressures, as the eastward fluid passes under (see the light blue profile which changes sign at pressures of approximately 10^{-3} bars). The equatorial jet in S3 and S4 extends over a somewhat larger pressure range than the high-latitude jets or the equatorial jet in S2, and also peaks at slightly higher velocities. At high latitudes in both S2 and S3 the opposing streams meet closer to the terminator east of the substellar point ($\phi = 90°$). Although some degree of subduction is seen in the yellow profiles, most of the fluid is pushed toward the equator, where significant down-welling occurs. The flow toward the equator can be seen near $\phi = 90°$ in Figure (3).

The transition in the overall flow structure (subduction vrs circumplanetary jet) between S2 and S3 can be related to the critical value of ν_{crit} for which viscous effects become comparable with advection. To quantify this we calculate a modified Reynolds number, where the length scales used for calculating the viscous and advective terms are different. We express the crossing timescale as $\tau_X = R_p/u_{avg}$ and the viscous timescale as $\tau_\nu = H_p^2/\nu$. We use the vertical scale-height H_p because we find in our simulations that the radial transfer of momentum ($\propto \frac{\partial u_\phi}{\partial r}$) is overwhelmingly the primary viscous sink for the jets as they traverse the planet. The ratio of τ_ν to τ_x gives our modified Reynolds number, Re. Averaging over the photosphere we find $H_p \sim 3 \times 10^7 cm$, $u_{avg} \sim 1km/s$, and $R_p \sim 9 \times 10^9 cm$. Setting $Re = 1$, we find that $\nu_{crit} \approx 10^{10} cm^2/s$ is the critical viscosity, above which viscous forces begin to dominate. For $\nu \geq \nu_{crit}$ viscous forces try and maintain the symmetry in the flows from both east and west. The flow patterns for S2 seen in Figure (4) represents the transition between advection dominated (simulations S3 and S4) and viscosity dominated (simulation S1) flows.

In Figure (5) we show the pressure-temperature profiles at the equator for all four simulations. The inversion at low pressures ($< 10^{-2}$ bars) and interior adiabat are both still clearly evident as seen in the radiative profile shown in Figure (1). Temperatures extend up to 2600K near the inner radial boundary, where the planet is spherically symmetric and fully convecting. Dayside temperature profiles (shown in red) are fairly consistent across all simulations S2-S4. The upper regions of S1 remain slightly hotter, with temperatures closer to the original radiative profile of Figure (1). The larger velocities calculated in S2-S4 are more effective at advecting away energy, cooling the dayside. However, the relative similarity between the dayside photospheric temperature of S2-S4 suggests that the profile of infrared and optical opacities (Equation (19)) is the dominant factor in determining dayside temperatures at pressures lower than 10^{-2} bars.

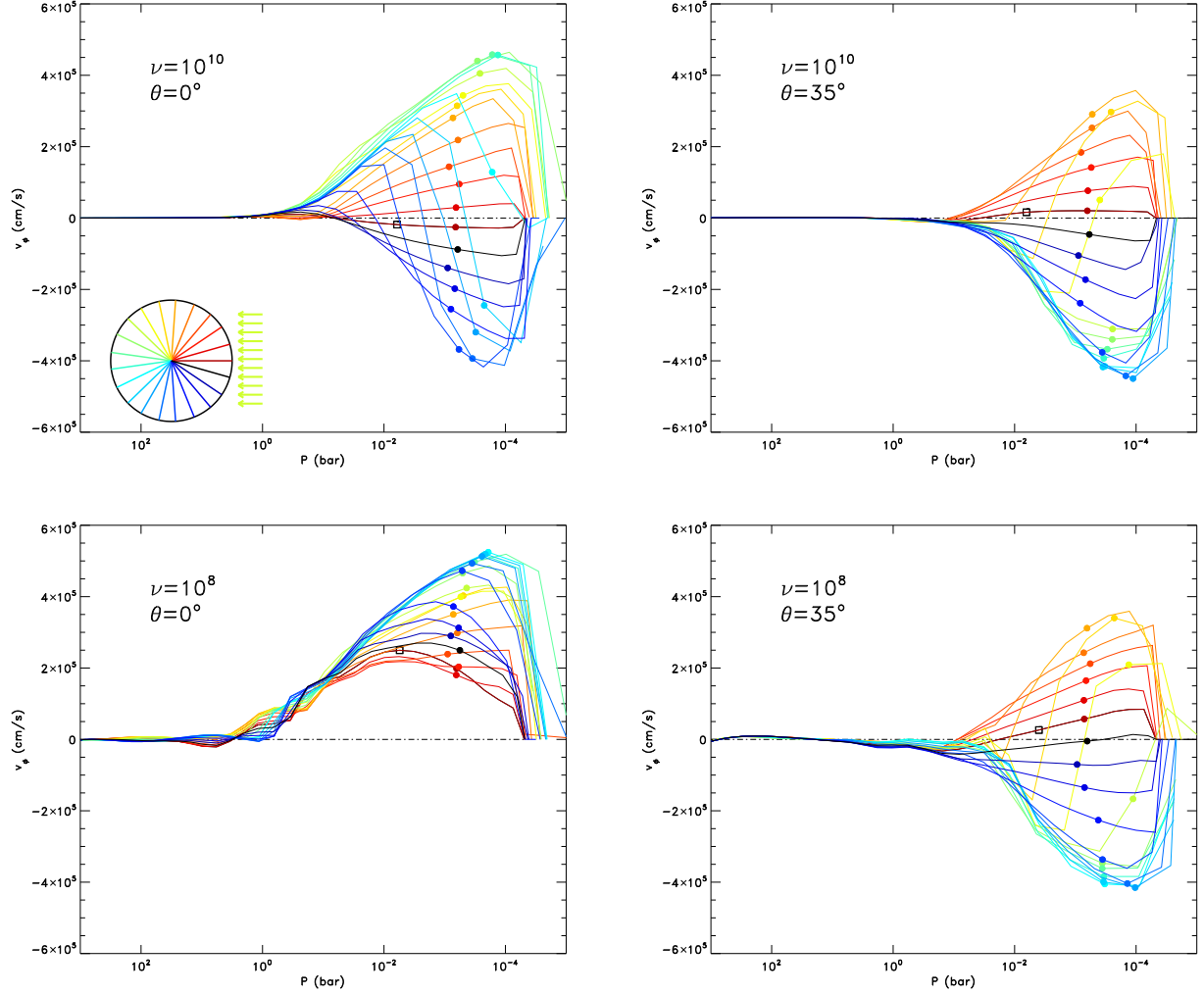The major effect of the fluid flow on the subsolar profile is at higher pressures, below both

Fig. 4.— The azimuthal velocity (cm/s) as a function of pressure at the equator for S2 (top row) and S3 (bottom row). The left column is a slice at the equator ($\theta = 0°$) and the right column is a slice at mid-latitudes ($\theta = 35°$). Profiles proceed from red at the sub-stellar longitude all the way around the planet in $18°$ steps in longitude. The key in the upper-left panel shows the longitudinal location of a given profile looking down the rotation axis, with the arrows indicating the direction of incident stellar flux. Solid dots denote the location of the infrared photosphere, while the square shows the location of the optical photosphere at the substellar point.

the optical and IR photospheres. The returning flow significantly cools the atmosphere at pressures around $1-10^{-2}$ bars creating a secondary, dynamically induced inversion at depth. The need for two inversions in the pressure/temperature profile, one caused by the different absorption and emission opacities and the other caused by the dynamics, was introduced in a parameterized manner by Burrows et al. (2007) in order to simultaneously match spectral constraints at multiple wavelengths. It arises self-consistently here. Comparing Figures (4) and (5), this cooler region is associated with the flow *returning* from the nightside after it has circumnavigated the planet and cooled while on the nightside. The final equilibrium temperature at this location will be determined by a balance between the incident energy diffusing downward from the optical photosphere and the advection bringing in cooler fluid from the nightside. For this reason, this secondary inversion is slightly warmer and narrower (in pressure) in S2, than in S3 or S4. As seen above, the higher viscosity (S2) limits flow velocities, giving the downward diffusing radiation more time to heat the fluid.

The differences between S2-S4 are most prominent at regions near the terminator east of the anti-stellar point (see the darker blue profile in Figure (5). The deep, fast jet of S4 cools the terminator east of the anti-stellar point ($\phi = 3\pi/2$) to a much greater extent then in any of the other simulations. This cooling produces a very distinct temperature inversion at this latitude. Such inversion features should be easily distinguishable in a spectra taken after primary transit but before secondary eclipse, when this terminator faces toward earth. In contrast, the terminator west of the anti-stellar point exhibits no inversion in any of the simulations.

The inclusion of viscosity in the governing equation provides another mechanism for converting kinetic energy back into thermal energy, regulating the velocity in the process. The left-hand plot of Figure (6) illustrates the strength of the viscous term $\left[\nu\nabla^2\mathbf{u} + \frac{\nu}{3}\nabla\left(\nabla\cdot\mathbf{u}\right)\right]_\phi$ in the longitudinal momentum equation for S2. This plot concentrates on the convergence region on the nightside, and clearly illustrates that viscosity primarily acts in this shear zone. Comparison to Figure (4) shows that the two shearing streams have relative velocities of up to 8km/s. The heads of the jets experience the greatest deceleration, reaching 1250cm/s^2. The importance of viscous dissipation on the overall energy distribution depends on its contribution to Equation (8). The other component making a major contribution to the thermal energy is the compressional work, $P\nabla\cdot\mathbf{u}$. Though for a majority of the atmosphere $P\nabla\cdot\mathbf{u}$ dominates, D_ν becomes more important in the convergence region for the lower viscosity simulations. In contrast, for the highest viscosity simulation S1, viscous heating is most relevant near the terminators where the velocities are highest. The right-hand plot shows the ratio of the viscous and compression terms on the nightside near the anti-stellar point. D_ν exceeds $P\nabla\cdot\mathbf{u}$ by several hundred times at the jet heads, which extend over a wide range in longitude. The details of this convergence region are paramount in determining the overall dynamical structure throughout the atmosphere, as it is here where flow either
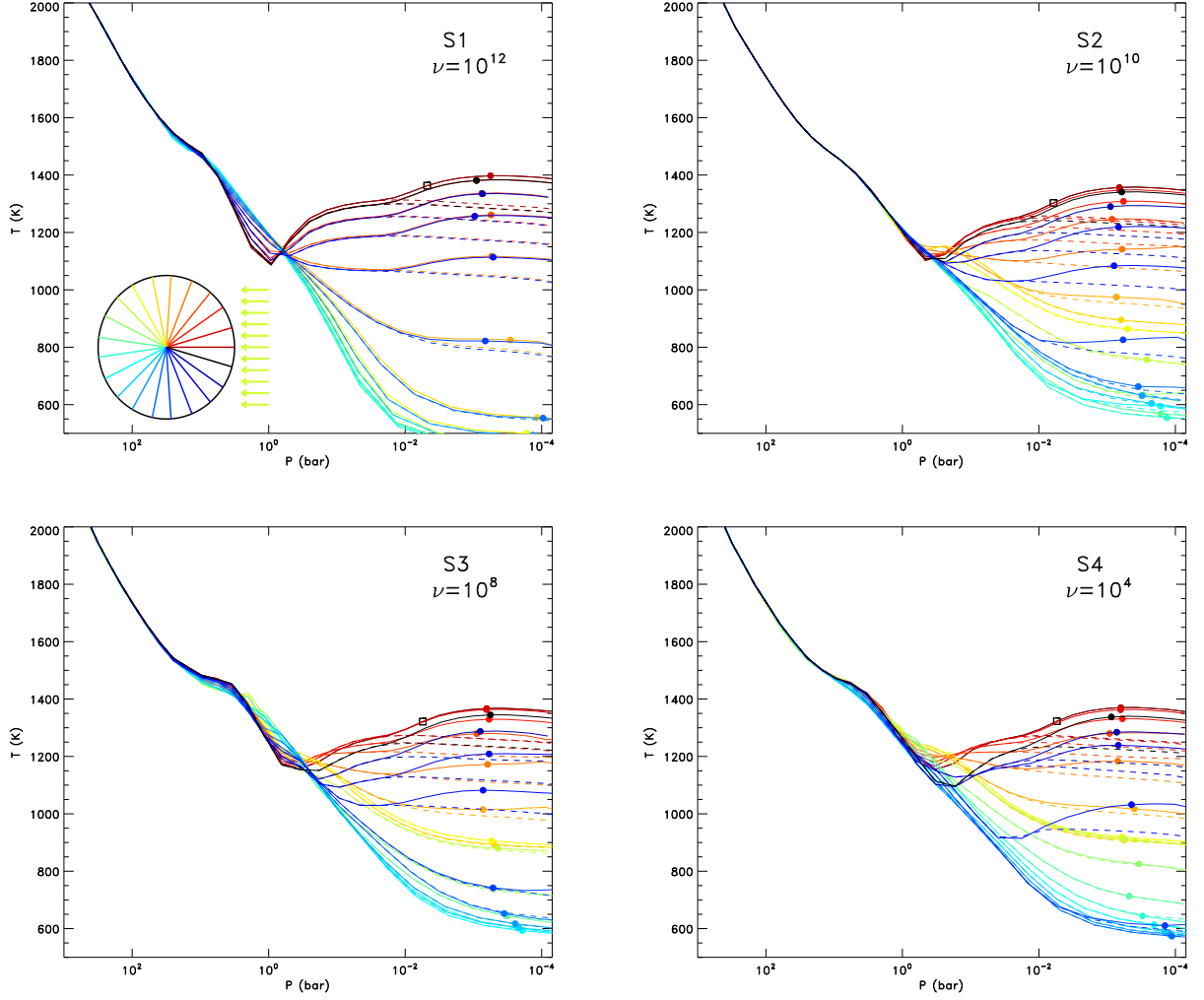
Fig. 5.— Temperature (solid lines) and radiation energy density $(E_R/a)^{1/4}$ (dashed lines) profiles as a function of pressure at the equator for S1-S4. Colors and symbols are as in Figure (4).

19

subducts under its counterpart or instigates circumplanetary jets. Neglecting the viscous contribution, especially in this region, may lead to erroneous results. Across all simulations, we find that the average ratio of D_ν to $P\nabla \cdot \mathbf{u}$ near the photosphere roughly scales with the value of the kinematic viscosity.

The relation between nightside temperature, velocity, and viscosity is important to understand. Many authors have noted that the nightside temperature can be understood by equating the crossing timescale with the radiative cooling timescale; larger velocities carry more energy to the nightside, decreasing the temperature differential, and thus the azimuthal acceleration. It is easy to see an equilibrium will quickly develop. The introduction of viscosity complicates the issue, controlling the velocity and heating the gas. Substantial viscous heating requires both shear and large ν. In S1, the high viscosity prevents flow to the nightside and thus viscous heating is confined to the dayside. Near the terminators D_ν exceeds $P\nabla \cdot \mathbf{u}$, but the energy is still dominated by the incident stellar heating, and the viscous contribution is insignificant. In contrast, there is significant shear on the nightside of S4, but, due to the low ν, D_ν is an order of magnitude smaller. S2 seems to be in a sweet spot. The viscosity is low enough to allow for shear flows to develop on the nightside, but high enough to still generate significant heating there.

3.3. Time Dependent Behavior: Exo-Weather

Although we have presented average quantities in the Section (3.2), the atmosphere can have a dynamic component super-imposed on the stationary background state. As described above, the background state consists of a quasi-stationary flow pattern with flows traveling in both eastward and westward directions. As a result, sustained supersonic winds traveling in opposite directions converge on the nightside in the upper atmosphere. Shocks, shearing, and instabilities result, and the location of the convergence point oscillates over a range of latitude and longitudes. The shock heating (D_ν) and compressional heating ($P\nabla \cdot \mathbf{u}$) associated with this convergence causes the temperature distribution on the nightside to fluctuate on the timescale of approximately half a day. Figure (7) shows the temperature distribution at the photosphere over a total of 1.5 days. As can be seen, flow variations drive temperature changes on the nightside, with the largest deviations occurring near the terminators.

Changes in the velocity structure are driven primarily by the interaction between high velocity shearing flows. Shearing occurs both between streams at constant pressure and also between different pressure layers. Shearing at constant pressure can be seen on the nightside in Figure (3) at $\pm 15°$ latitude for S2-S4 where eastward and westward material pass by each-other and interact. Shearing between flows at different pressure levels can be seen in Figure

(4), where the subducting material travels under counter-flowing material. This can be seen at $\theta = 35°$ for S2 and S3, and additionally at the equator for S2. We find that variations in the temperature at the photosphere are principally driven by the subduction at the equator, as eastward moving material sinks below westward moving material at $\phi \sim 3\pi/2$. Significant potential vorticity is generated in this subduction region, with vortices forming between the two shearing flows. As the convergence point moves across the surface it forces these vortices to interact, stirring temperatures further, both at the photosphere and at depth. Over the course of the entire simulation the location of the coldest point in the calculated phase-curve is seen to oscillate more than 20° in longitude, occasionally shifting to the west of the anti-stellar point. The largest temperature variations (up to 15%) are seen along the terminators, where changes to flow patterns have the largest impact on advective efficiencies.

4. Enthalpy, Radiation, and Kinetic Energy Fluxes

One important, overarching questions for groups that model the atmospheric dynamics of hot-Jupiters is calculating how much energy is transferred to the nightside, and how changing conditions change the resulting dynamics and energy distribution. In a recent article Goodman (2008) points out that without viscosity the atmosphere will adjust to a different solution in order to achieve a steady state with zero Carnot efficiency. This is fundamentally an argument regarding the momentum equation, not the energy equation. To illustrate this, consider the momentum equation (1) in steady state, neglecting rotation. Taking the dot product with velocity and expressing the advective term as $(\mathbf{u} \cdot \nabla) \mathbf{u} = 1/2\nabla |\mathbf{u}|^2 + (\nabla \times \mathbf{u}) \times \mathbf{u}$, we can write

$$\mathbf{u} \cdot \nabla \left(\frac{1}{2} |\mathbf{u}|^2 + w + \phi_g \right) = \mathbf{u} \cdot T\nabla S + \mathbf{u} \cdot \nu\nabla^2\mathbf{u} + \mathbf{u} \cdot \frac{\nu}{3}\nabla (\nabla \cdot \mathbf{u}). \tag{20}$$

The term in parenthesis is the Bernoulli constant (E_B) of the flow, S is the entropy per unit mass, and $w = \epsilon/\rho + P/\rho$ is the enthalpy per unit mass. Bernoulli's constant is the total of the kinetic, thermal, and potential energies. Next consider the steady state form of the two energy Equations (7) and (8), which together become

$$(\mathbf{u} \cdot \nabla)\epsilon = -P\nabla \cdot \mathbf{u} - \nabla \cdot \mathbf{F} + S_\star + D_\nu. \tag{21}$$

$S_\star = \rho\kappa_\star (T, P) F_\star e^{-\tau_\star}$ is the direct stellar energy absorbed by the gas. Utilizing the first-law of thermodynamics, this can be expressed as

$$\mathbf{u} \cdot T\nabla S = \rho^{-1} [D_\nu - \nabla \cdot \mathbf{F} + S_\star], \tag{22}$$

where the $P\nabla \cdot \mathbf{u}$ term cancels out, as this does not contribute to changes in entropy. Plugging this into Equation (20) we see that the gradient of E_B along streamlines is

$$\mathbf{u} \cdot \nabla E_B = \rho^{-1} [D_\nu - \nabla \cdot \mathbf{F} + S_\star] + \mathbf{u} \cdot \nu\nabla^2\mathbf{u} + \mathbf{u} \cdot \frac{\nu}{3}\nabla (\nabla \cdot \mathbf{u}). \tag{23}$$

However, the role of viscosity here is to convert kinetic energy to thermal energy. Therefore, the viscous contribution from the momentum equation must be equal and opposite to the viscous contribution from the energy equation ($\rho^{-1} D_\nu = -\mathbf{u} \cdot \nu \nabla^2 \mathbf{u} - \mathbf{u} \cdot \frac{\nu}{3} \nabla (\nabla \cdot \mathbf{u})$) leaving us with

$$\mathbf{u} \cdot \nabla E_B = \rho^{-1} \left[S_\star - \nabla \cdot \mathbf{F} \right]. \tag{24}$$

Changes in the gradient of E_B along a streamline are solely due to radiation effects, even when viscosity is included. Since the integral of $\mathbf{u} \cdot \nabla E_B$ around a closed streamline must equal zero in steady-state, so too must the radiation terms. Therefore, the important difference when including viscosity is the behavior of the streamlines. Including viscosity will alter the velocity, changing the streamlines and thus also the overall thermal structure of the atmosphere. Figures (3) and (4) show that viscosity can play an important role in altering the velocity (and thus thermal) structures for the planetary atmosphere. Ultimately, Equation (24) tells us that the direct effects of viscosity are important for solving the momentum equation, not the energy equation, further justifying our choice to solve the full 3D Navier-Stokes equations.

As pointed out by Goodman (2008), another way to understand the importance of viscosity is to calculate the relative importance of the longitudinal energy fluxes carried as kinetic energy vs that carried as enthalpy. The left-hand panel of Figure (8) compares the azimuthal flux of enthalpy ($\epsilon/\rho + P/\rho$) to the azimuthal flux of kinetic energy ($|\mathbf{u}|^2/2$). Energy carried in the form of enthalpy dominates that carried in kinetic energy form throughout most of the interior. However, at higher altitudes the two contributions become comparable. In particular, in regions of high velocities on the nightside, where we have already seen that shocks play a role in determining the dynamical structure, the flux of kinetic energy exceeds that of enthalpy. In these regions energy is primarily carried in kinetic form and energy loss through shocks is important. Our approach of integrating the Navier-Stokes equations allows us to follow the transfer energy from kinetic to internal energy across shocks even if the shocks themselves are not fully resolved. As emphasized by Goodman (2008), this in not the case for more simplified treatments of the dynamics.

One final advantage of the method we are using here is that radiation is allowed to flow in all three dimensions. Incident radiation is modeled here as being purely radial, but re-radiated photons can also carry energy both to the nightside and pole-ward. Although the radial component is by far the most important, at high altitudes with pressures less than ~ 0.01 bars, the azimuthal flux of radiation can become comparable to the radial radiative flux. The ratio of $\mathbf{F}_r$ to $\mathbf{F}_\phi$ to is shown in the right-hand plot of Figure (8). Although never exceeding the radial radiative flux, the azimuthal radiative flux is of the same order throughout the dayside and extending to the terminators. The effects of the azimuthal radiative transfer are most prominent near the terminators, where they play a

role in shaping the final pressure-temperature profiles.

5.   Conclusion

We have performed a series of simulations for the atmosphere of the highly irradiated planet HD209458b. Our approach involves solving the full 3D Navier Stokes equation coupled to both the thermal and radiative energy equations. We have separated our frequency averaged opacities into those relevant for incoming stellar photons and those for re-radiated photons. This approach allows us to reproduce the observed temperature inversion in the upper atmosphere and self-consistently calculate the location that stellar energy is deposited. This deposited energy drives flow in both the eastward and westward directions, with eastward flow concentrated near the equator and westward flow pushed to higher latitudes above and below the equator. These flows then converge on the nightside and exhibit range of behavior for various explicit turbulent viscosities.

The viscosity in our simulations spans a wide range, running from $\nu = 10^{12}$ to $10^4 \text{cm}^2/\text{s}$, corresponding to effective $\alpha_{eff,ph}$-parameters ranging from approximately 10^{-1} to 10^{-9}. As expected, results vary significantly with viscosity, especially for higher viscosities. For our highest viscosities, atmospheric velocities remained subsonic, advection of energy is suppressed, and the day-night temperature contrast remains high. As viscosity is decreased flow velocities became super-sonic, reaching speeds of over 5km/s in the lowest viscosity simulation. In addition to the speed, the behavior of the jets significantly changes with viscosity. For the simulations with low viscosity ($\alpha_{eff,ph} = 10^{-5}$ and 10^{-9}) a jet develops that circumnavigates the planet at a single pressure near the equator. However for intermediate viscosity ($\alpha_{eff,ph} \approx 10^{-3}$), and at high/low latitudes in all simulations, circumplanetary flow of a jet can only be achieved accompanied by subduction. Subduction occurs as the fluid cools and sinks radially, crossing isobars.

Viscosity also plays a role in determining the variability of the atmospheric flows and energy distribution. This variability manifests itself in two ways: temporally varying velocity structures that alter advection efficiency, and through viscous heating. Seen most prominently in the simulation with $\nu = 10^{10} cm^2/s$ (S2), shearing between converging flows on the nightside in both the horizontal and radial directions drives oscillations in the flow patterns. These oscillations alter the location of the convergence point and shape of the streamlines thus changing the rate of energy advection coming from the dayside, primarily affecting the temperature near the terminators on the level of 15%. Changing streamlines also shift the region of maximum shear, in turn altering the location of hot-spots on the nightside induced by viscous heating. The location of the coldest point in the calculated phase curve can shift by more than 20° in longitude, occasionally even appearing west of

the anti-stellar point. Such time-dependent behavior is somewhat suppressed in our other simulations (S1, S3, and S4). Viscously driven variations in the flow require that the viscous term ($\nu\nabla^2\mathbf{u}$) in the momentum equation be of order the advective term (($\mathbf{u}\cdot\nabla)\mathbf{u}$). This only occurs for sufficiently high shear (present for low-ν simulations) and also large enough kinematic viscosity (ν). The $\nu = 10^{10}cm^2/s$ simulation exists in somewhat of a sweet-spot, allowing high velocity flows and still maintaining significant viscous heating on the nightside. Such variation, if observed, may provide a clue to the nature of the turbulent viscosity in close-in giant planet atmospheres.

Fluctuations in velocity and temperature are largely confined to the nightside. Periodic dynamical variations on the dayside are not able to alter the basic structure at an observable level due to the dominant incident stellar flux. This is a somewhat different result then the simulations of Cho et al. (2003, 2008); Rauscher et al. (2008) and Menou & Rauscher (2008), where they demonstrate significant variations throughout the entire phase-curve for a range of selected parameters. The variations in their models are largely due to cold circumpolar vortices, though they do observe smaller amplitude variations near the equator. We do not see such cold circumpolar vortices, though their development may be impeded due to our longitudinal boundary conditions. Variations driven by large scale vortices are considerably different in nature then those presented here, which arise from the shearing between converging flows and are confined primarily to the nightside. We find, apart from a modest downwind advection of the hot-spot, dynamics does very little to alter the temperature profiles very high in the atmosphere on the dayside. Simulations with high velocity winds cool the upper atmosphere slightly, but the final temperatures are fairly similar to the radiative simulations. The pressure-temperature profile at pressures less than 10^{-2} bars is thus primarily dependent on our choice of opacity and its behavior with depth as originally shown by Hubeny et al. (2003). With a lack of better knowledge concerning the abundance of high opacity sources such as TiO or VO, we have chosen to augment the opacity with an ad-hoc extra source at high pressures (Burrows et al. 2008). For comparison, the models of HD209458b by Showman et al. (2009) include TiO and VO in the calculation of opacity, and as a result of this larger $\kappa_\star(T,P)$ achieve much higher temperatures at high altitude. Given that this extra opacity is the dominant factor in determining the temperature, matching future observations for a wide range of temperatures requires only adjusting the magnitude of this opacity. Temporal variation in this opacity would drive variations in dynamics, though Agol et al. (2008) studied a series of secondary eclipse of HD189733b and find that a variation in $F_{day}/F_\star$ of less then 10%, consistent with a stable dayside temperature. Transit spectroscopy appears to be the most promising observational technique for constraining exo-weather.

The implications of dynamical behavior across the nightside is clear; it changes the temperature and location of the coldest spot, and it changes the temperature structure

near the terminators. The concentration of the fluctuations near the equator serves to enhance the observability of such variations. Average nightside temperatures, important for constraining interior and evolutionary models, can only be obtained by averaging a number of such observations. This result also suggests a possible interpretation for the puzzling results seen by Knutson et al. (2007), in which they observe a local minimum in the flux *before* the secondary eclipse for HD 189733b. Though we have no simulated this planet, in light of the dynamical behavior seen in our simulations the increase in flux before secondary eclipse may be attributed to transient exo-weather, which shifts the shape of the planets phase-curve over time.

REFERENCES

Agol, E., Cowan, N. B., Bushong, J., et al. 2008, ArXiv e-prints

Burkert, A., Lin, D. N. C., Bodenheimer, P. H., Jones, C. A., & Yorke, H. W. 2005, ApJ, 618, 512

Burrows, A., Budaj, J., & Hubeny, I. 2008, ApJ, 678, 1436

Burrows, A., Hubeny, I., Budaj, J., Knutson, H. A., & Charbonneau, D. 2007, ApJ, 668, L171

Cho, J. Y.-K., Menou, K., Hansen, B. M. S., & Seager, S. 2003, ApJ, 587, L117

—. 2008, ApJ, 675, 817

Cooper, C. S. & Showman, A. P. 2005, ApJ, 629, L45

—. 2006, ApJ, 649, 1048

Dobbs-Dixon, I. & Lin, D. N. C. 2008, ApJ, 673, 513

Goodman, J. 2008, ArXiv e-prints

Howell, L. H. & Greenough, J. A. 2003, Journal of Computational Physics, 184, 53

Hubeny, I., Burrows, A., & Sudarsky, D. 2003, ApJ, 594, 1011

Kley, W. & Hensler, G. 1987, A&A, 172, 124

Knutson, H. A., Charbonneau, D., Allen, L. E., Burrows, A., & Megeath, S. T. 2008, ApJ, 673, 526

Knutson, H. A., Charbonneau, D., Allen, L. E., et al. 2007, Nature, 447, 183

Langton, J. & Laughlin, G. 2007, ApJ, 657, L113

—. 2008, ApJ, 674, 1106

Levermore, C. D. & Pomraning, G. C. 1981, ApJ, 248, 321

Mazeh, T., Naef, D., Torres, G., et al. 2000, ApJ, 532, L55

Menou, K. & Rauscher, E. 2008, ArXiv e-prints

Milhalas, D. & Milhalas, B. 1984, Foundations of Radiation Hydrodynamics (Dover Publications, Inc.)

Moses, J. I., Fouchet, T., Bézard, B., et al. 2005, Journal of Geophysical Research (Planets), 110, 8001

Ogilvie, G. I. & Lin, D. N. C. 2004, ApJ, 610, 477

Penev, K., Barranco, J., & Sasselov, D. 2008, ArXiv e-prints

Rauscher, E. & Menou, K. 2009, ArXiv e-prints

Rauscher, E., Menou, K., Cho, J. Y.-K., Seager, S., & Hansen, B. M. S. 2008, ApJ, 681, 1646

Sharp, C. M. & Burrows, A. 2007, ApJS, 168, 140

Showman, A. P., Cooper, C. S., Fortney, J. J., & Marley, M. S. 2008a, ApJ, 682, 559

Showman, A. P., Fortney, J. J., Lian, Y., et al. 2009, ApJ, 699, 564

Showman, A. P. & Guillot, T. 2002, A&A, 385, 166

Showman, A. P., Menou, K., & Cho, J. 2008b, 398, 419

Spiegel, D. S., Silverio, K., & Burrows, A. 2009, ApJ, 699, 1487

Stone, J. M. & Norman, M. L. 1992, ApJS, 80, 753

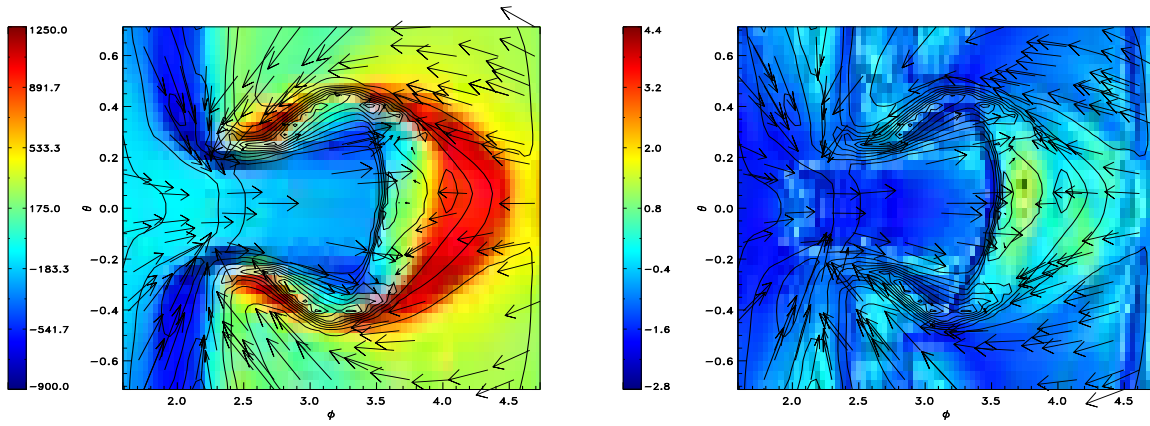Zahnle, K., Marley, M. S., Freedman, R. S., Lodders, K., & Fortney, J. J. 2009, ArXiv e-prints

Fig. 6.— The azimuthal component of the viscous force at the photosphere (left), acting on u_ϕ. The right panel shows the ratio of viscous and compression contributions, plotted as $log_{10}\left(|D_\nu/P\nabla\cdot\mathbf{u}|\right)$. Both graphs are contoured with the total velocity at the photosphere and are for S2, with $\nu = 10^{10}\mathrm{cm}^2/\mathrm{s}$. We have zoomed into the region on the nightside centered on the anti-stellar point with the equator running horizontally through $\theta = 0$, to better illustrate this crucial region.
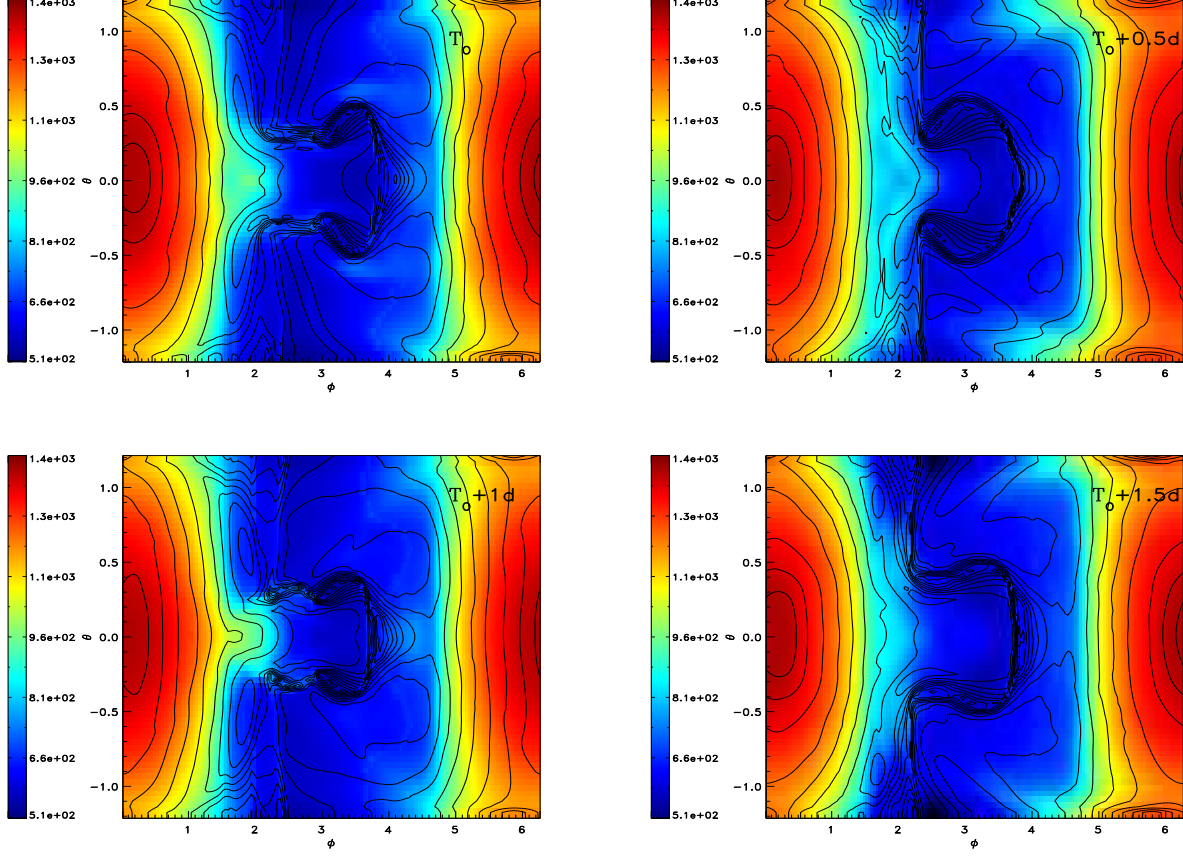
28

Fig. 7.— The time dependence of S2 ($\alpha_{eff,ph} = 10^{-3}$). Snapshots are shown half a day apart and illustrate temperature (color scale) and total velocity (contours). Radial and horizontal shearing drives variations in the flow, changing the advection of energy across the terminators and influencing the location of viscous dissipation.
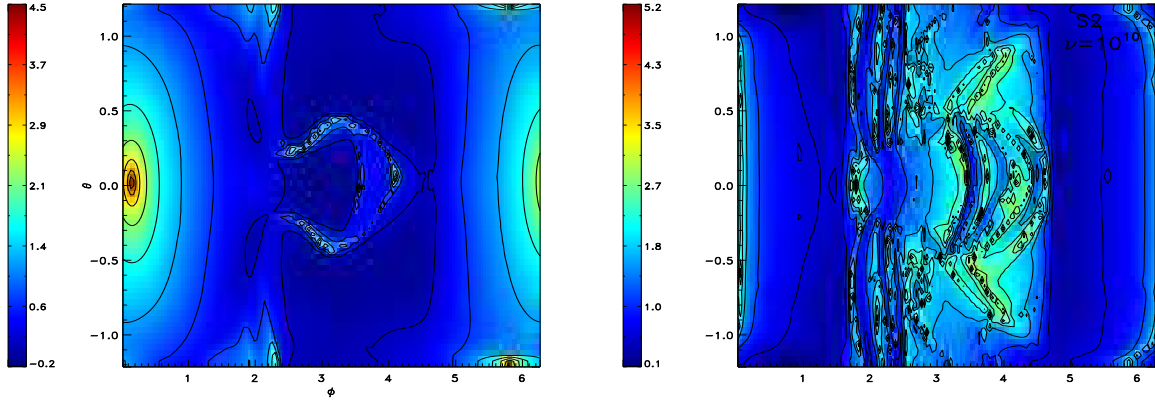
Fig. 8.— The ratio of enthalpy and kinetic fluxes throughout the photosphere (left panel). In regions with $F_K > F_E$, it is important to include viscous effects. The right panel show the ratio of the radial to azimuthal radiative energy flux. Azimuthal radiative transport becomes particularly important near the terminators. Both plots are shown as the logarithm of the absolute value of the flux ratios and are for S2.